ELSEVIER

Journal of Wind Engineering
and Industrial Aerodynamics 62 (1996) 131–161

JOURNAL OF
wind engineering
AND
industrial
aerodynamics

Two-dimensional simulation of flow around rectangular prisms

D. Yu, A. Kareem*

Department of Civil Engineering and Geological Sciences, University of Notre Dame, Notre Dame, IN 46556-0767, USA

Received 11 April 1996; revised 10 October 1996; accepted 23 October 1996

Abstract

Pressure and velocity fields around rigid prisms of rectangular cross-section are numerically simulated for a Reynolds number of 10^5 using the large eddy simulation (LES). In conjunction with LES, a finite difference scheme is employed on the basis of a staggered grid, in which the convection terms are discretized by the QUICK scheme. The outflow boundary condition is then satisfied by the convection condition. This numerical scheme combined with the LES model offers a computationally efficient tool for simulating high Reynolds number flows around bluff bodies. The LES scheme employed in this study may be viewed as a coherent structure capturing technique to distinguish it from a true LES in which the scales are generally resolved to very small size. The numerical scheme is applied to calculate both the instantaneous velocity and the pressure fields over the entire domain. In addition, the mean and root mean square (RMS) values, the power spectra of the pressure fluctuations on the prism surface, the integral forces (lift and drag forces) and probability densities of pressure fluctuations are presented. Additional calculations concerning the chordwise correlation of pressure around the square prism and its eigenfunction expansion are presented. Simulated results, including the mean velocity along the symmetry line, are then compared with the available experimental data and numerical results by other investigators. With the exception of the lift and drag force spectra whose values do not match closely, and the probability densities for which no experimental data were available, all other features are observed to be in good agreement with experimental findings. Streaklines are also employed to visualize the flow field around rectangular prisms and are found to match the vorticity contour of the flow field. Streakline sequences clearly demonstrate the shedding of two vortices in every cycle of the integral lift force on the bluff body. The separation–reattachment features on the side faces of rectangular prisms are also visualized. A parametric study concerning bodies of different aspect ratios illustrates clearly the modifications in the flow field patterns which are sensitive to the streamwise length of the body and the associated pressure distribution.

* Corresponding author.

PII S0167-6105(96)00076-1

Keywords: Turbulence; Bluff body aerodynamics; Large eddy simulation; Numerical methods; Streaklines; Pressure fluctuation; Wind-structure interaction; Wind loads; Drag coefficient; Lift coefficient; Power spectral density; Probability density function; Correlation; Eigenfunction

1. Introduction

The study of wind–structure interaction has fundamental implications to engineering problems (e.g., the effect of wind on bridges, buildings, offshore facilities and motor vehicles). In the structural engineering area, wind-induced loads on structures often introduce concerns related to both the integrity of structural envelope and the safety of the overall structural system. Although the knowledge of wind effects on structures has significantly improved in recent decades, an understanding of the nonlinear interactions that take place as wind encounters structures has not been developed in enough detail to develop functional relationship. Not only is the wind approaching a building complex, but also the flow patterns generated around a structure are complicated by the distortion of the mean flow field, flow separation, vortex formation, and wake development. Such effects have precluded theoretical treatment of the problem. Thus, emphasis has been placed on physical modeling of fluid–structure interactions, which offers an accurate means of acquiring pressure and load fluctuations on structures. Presently, such models utilize boundary layer wind tunnels to study the characteristics and ramifications of complex, turbulent, boundary layer winds flowing over various structural configurations.

Recently, due to advances in computational fluid dynamics, combined with the availability of more powerful computers, the numerical modeling of flow around structures has become an attractive alternative to physical modeling. Numerical modeling in wind engineering is based on methods of computational fluid dynamics (CFD). Coupled with computer aided flow visualization, which provides visual animation, the numerical simulation may serve as a useful tool to analyze the evolution of flow field around structures and the attendant load effects. These techniques are presently in developmental stage and are computationally quite intensive, and like any other modeling procedure, they are not free from error. In wind-related problems, issues concerning space and the discretization, turbulence modeling, atmospheric boundary layer simulation, and modeling of appropriate inflow conditions require further investigation before numerical modeling attains practical status. Accordingly, the development of numerical techniques that provide realistic definition of the flow around a body will provide a valuable additional tool that may be used in design of buildings and other structures. In addition, such a numerical analysis tool, which can run efficiently on computers available to design firms, would make it possible to evaluate a host of design configurations in the preliminary design stage, while using a boundary layer wind tunnel for the determination of the final design.

The flow field is modeled by the Navier–Stokes equations with appropriate boundary conditions. Turbulence models have been developed to simulate high Reynolds

number flows that are not achievable with direct numerical simulation (DNS) due to computer limitations or to simulate a flow with the same Reynolds number similar to DNS but with less computational effort. Currently, the most widely used turbulence model is the k–ε method, which has the advantage of lower computational effort, but with a lower level of accuracy [1–4]. The LES approach has emerged as a more attractive scheme which has the promise of providing improved results with reasonable computational effort. In LES, fluid motion scales larger than the filter size are resolved and solved directly, while the scales smaller than the filter size are modeled by a subgrid-scale model [5]. The most commonly used LES simulation relies on the Smagorinksy model for subgrid-scale viscosity [6,7]. A detailed, critical review of the LES technique as well as other options can be found in review papers by Boris et al. [8], Ferziger [5], Mason [9], and Lesieur and Metais [10]. Coherent flow structures are responsible for the large-scale pressure field; therefore, a scheme that models essentially coherent structures is appropriate for wind engineering applications. It is referred to as coherent structure capturing (CSC) to distinguish it from classical LES approach [5]. One should not expect CSC to simulate flow field characteristics that are associated with scales smaller than the filter length used in LES model. The CSC is essentially a subset of LES in which the filter size is larger than that used in typical LES simulations.

All numerical studies rely on a good numerical scheme for the evaluation of the parameters in the sample space. Many numerical methods have been developed over the years which include the finite difference method, finite element method, and spectral method, each with its own advantages and disadvantages. Regardless of the choice of method, the convection term must be properly discretized to insure both accuracy and stability. Generally, the scheme should have at least accuracy of second order, since lower-order schemes may introduce artificial viscosity which may exceed the turbulence viscosity designed in LES. A proper definition of boundary conditions is also very important. In wind-engineering-related applications, the flow field extends to infinity in one or more directions, thus requiring an artificial outflow boundary to keep the simulated domain finite. This kind of boundary requires more scrutiny, because a free boundary condition, $\partial/\partial n = 0$, may not be well justified. On solid wall boundaries, when the grid resolution is not fine enough to resolve the boundary flow, an artificial boundary condition may also be necessary [11].

Murakami and his team conducted a series of numerical studies involving 2D square cylinders and a cube fixed to the ground [12–17]. They also compared the numerical results of the k–ε model and the LES with wind tunnel results [1], and generally found that three-dimensional modeling provides a better representation of the flow characteristics than the two-dimensional case. Their LES modeling of the flow field also provided an improved and more realistic simulation of the flow fields in comparison with k–ε based simulation.

In this paper, plane flows with zero incidence attack angle over two-dimensional prisms of rectangular cross-section are numerically simulated at a Reynolds number of 10^5, using LES, or more appropriately CSC scheme. Computational scheme involves a finite difference method utilizing a staggered grid on which the convection terms are discretized by a third-order QUICK scheme [18]. The temporal marching is

accomplished by a Leith-type method. The pressure is calculated using a separate equation and applying the successive overrelaxation (SOR) method. Utilization of the LES model permitted calculations of both the instantaneous velocity and pressure fields over the entire domain at high Reynolds numbers. For the velocity field, the mean velocity along the symmetry line is computed and compared to experimental and other numerical results. Mean and RMS pressure distributions, power spectra, spatial correlation, and integral forces on the prism (lift and drag forces) are also derived and compared with the available experimental results. In addition, streaklines are drawn to visualize the separation and reattachment of the flow and vortex shedding patterns.

2. Theoretical and numerical background

2.1. Governing equations

The Navier–Stokes equations for an incompressible fluid combined with a subgrid scale turbulence viscosity model are used for the large eddy simulation (LES) of the flow around a rectangular prism [7, 12–17]. In this study, the Smagorinsky model is used for the subgrid-scale viscosity [6]. The governing equations are

$$\frac{\partial \bar{u}_i}{\partial t} + \bar{u}_j \frac{\partial \bar{u}_i}{\partial x_j} = -\frac{1}{\rho}\frac{\partial \bar{P}}{\partial x_i} + \frac{\partial}{\partial x_j}(\nu + \nu_{SGS})\bar{s}_{ij}, \tag{1}$$

$$\frac{\partial \bar{u}_i}{\partial x_i} = 0, \tag{2}$$

$$\nu_{SGS} = (C_s \Delta)^2 \left[\tfrac{1}{2}\bar{s}_{ij}\bar{s}_{ij}\right]^{1/2} \tag{3}$$

and

$$\bar{s}_{ij} = \frac{\partial \bar{u}_i}{\partial x_j} + \frac{\partial \bar{u}_j}{\partial x_i}, \tag{4}$$

where $i,j = 1,2$ for the two-dimensional computation in this paper. $\bar{u}_i$ and $\bar{P}$ are the large-scale velocity and pressure, and ν is kinematic viscosity of the fluid. Eq. (3) is the Smagorinsky model which defines subgrid-scale viscosity ν_{SGS}, where $\Delta = (\mathrm{D}x_1\,\mathrm{D}x_2)^{1/2}$ and $C_s = 0.15$ are used.

These equations are non-dimensionalized using the length of the front side of the rectangular cross section L, and the inflow velocity U_0. Then time is non-dimensionalized by L/U_0 and pressure with ρU_0^2, where ρ is the mass density of the fluid. The Reynolds number is thus defined as LU_0/ν, with ν being the fluid kinematic viscosity.

2.2. Numerical scheme

In this simulation, the primitive variable formulation is used, while the computational domain is discretized with a staggered grid such as the marker and cell (MAC)

method [19]. In studies involving a subgrid-scale turbulence viscosity model, it is important that the accuracy order of the finite difference scheme be high enough to ensure that the numerical diffusion caused by the discretization will not dwarf the turbulence viscosity. Such being the case, a third-order, upwind difference scheme for the convection terms in conjunction with the Leith-type scheme for the temporal marching, following the method of Davis and Moore [20,21], are applied. The discretization algorithm has been integrated with the LES model so that the characteristics of high Reynolds number flows are captured.

The one-dimensional convection diffusion equation, using ϕ to represent velocity in x_1 or x_2 direction at a discretized grid point, yields

$$\frac{\partial \phi}{\partial t} + U\frac{\partial \phi}{\partial x} = \Gamma\frac{\partial^2 \phi}{\partial x^2}, \tag{5}$$

where Γ includes the viscosity due to the fluid property and the subgrid-scale model. From this equation,

$$\frac{\partial^2 \phi}{\partial t^2} \simeq U^2\frac{\partial^2 \phi}{\partial x^2} - 2U\Gamma\frac{\partial^3 \phi}{\partial x^3} \tag{6}$$

and

$$\frac{\partial^3 \phi}{\partial t^3} \simeq -U^3\frac{\partial^3 \phi}{\partial x^3}. \tag{7}$$

Utilizing the Taylor expansion, we obtain

$$\phi^{N+1} = \phi^N + \Delta t\left.\frac{\partial \phi}{\partial t}\right|^N + \frac{1}{2}\Delta t^2\left.\frac{\partial^2 \phi}{\partial t^2}\right|^N + \frac{1}{6}\Delta t^3\left.\frac{\partial^3 \phi}{\partial t^3}\right|^N + \mathrm{O}(\Delta t^4). \tag{8}$$

Substituting Eqs. (5)–(7) into Eq. (8) yields

$$\phi^{N+1} = \phi^N + \Delta t\left(-U\frac{\partial \phi}{\partial x} + \Gamma\frac{\partial^2 \phi}{\partial x^2}\right)\Bigg|^N + \frac{1}{2}\Delta t^2\left(U^2\frac{\partial^2 \phi}{\partial x^2} - 2U\Gamma\frac{\partial^3 \phi}{\partial x^3}\right)\Bigg|^N + \frac{1}{6}\Delta t^3\left(-U^3\frac{\partial^3 \phi}{\partial x^3}\right)\Bigg|^N + \mathrm{O}(\Delta t^4). \tag{9}$$

ϕ^N defined here may be considered as an average value centered at a grid point i, overlapping the length of a grid size Dx, and the values of ϕ_i^N in numerical calculation are defined at the ith grid node. Thus, by fitting a parabolic curve to the points at the $(i-1)th$, ith, and $(i+1)$th grid nodes, and integrating over the length of a grid centered at the ith grid, it yields

$$\phi^N = \phi_i^N + \frac{1}{24}(\phi_{i-1}^N - 2\phi_i^N + \phi_{i+1}^N) \simeq \phi_i^N + \frac{\Delta x^2}{24}\frac{\partial^2 \phi}{\partial x^2} \tag{10}$$

or

$$\phi^{N+1} - \phi^N \simeq \phi_i^{N+1} - \phi_i^N + \frac{\Delta x^2\,\Delta t}{24}\frac{\partial^2}{\partial x^2}\left(\frac{\partial \phi}{\partial t}\right), \tag{11}$$

but from Eq. (5),

$$\frac{\Delta x^2 \Delta t}{24}\frac{\partial^2}{\partial x^2}\left(\frac{\partial \phi}{\partial t}\right) \simeq -\frac{U \Delta x^2 \Delta t}{24}\frac{\partial^3 \phi}{\partial x^3},$$

so

$$\phi_i^{N+1} - \phi_i^N \simeq \phi^{N+1} - \phi^N + \frac{1}{24} U \Delta x^2 \Delta t \frac{\partial^3 \phi}{\partial x^3}. \tag{12}$$

Combining with Eq. (9),

$$\phi_i^{N+1} \simeq \phi_i^N - \Delta t U \frac{\partial \phi}{\partial x} + \left(\Delta t \Gamma + \frac{\Delta t^2 U^2}{2}\right)\frac{\partial^2 \phi}{\partial x^2} - \left(\Delta t^2 U \Gamma + \frac{\Delta t^3 U^3}{6} - \frac{1}{24} U \Delta t \Delta x^2\right)\frac{\partial^3 \phi}{\partial x^3}. \tag{13}$$

Now the convection terms are discretized by the QUICK scheme [18] and the diffusion term by a central difference scheme. For $U > 0$, these schemes are listed below:

$$\frac{\partial \phi}{\partial x} \simeq \frac{1}{\Delta x}\left\{\left[\frac{1}{2}(\phi_i + \phi_{i+1}) - \frac{1}{8}(\phi_{i-1} - 2\phi_i + \phi_{i+1})\right] - \left[\frac{1}{2}(\phi_{i-1} + \phi_i) - \frac{1}{8}(\phi_{i-2} - 2\phi_{i-1} + \phi_i)\right]\right\},$$

$$\frac{\partial^2 \phi}{\partial x^2} \simeq \frac{1}{\Delta x^2}(\phi_{i-1} - 2\phi_i + \phi_{i+1}),$$

$$\frac{\partial^3 \phi}{\partial x^3} \simeq \frac{1}{\Delta x^3}(\phi_{i+1} - 3\phi_i + 3\phi_{i-1} - \phi_{i-2}).$$

Substituting into Eq. (13), and noting $C = U\Delta t/\Delta x$, $\gamma = \Gamma \Delta t/\Delta x^2$,

$$\phi_i^{N+1} = \phi_i^N - \tfrac{1}{2}C(\phi_{i+1}^N - \phi_{i-1}^N) + (\gamma + \tfrac{1}{2}C^2)(\phi_{i+1}^N - 2\phi_i^N + \phi_{i-1}^N) + C(\tfrac{1}{6} - \gamma - \tfrac{1}{6}C^2)(\phi_{i+1}^N - 3\phi_i^N + 3\phi_{i-1}^N - \phi_{i-2}^N). \tag{14}$$

If the mixed derivatives are all omitted, then the 2D algorithm is a direct extension of the 1D formula [20,21]; thus the discretized 2D equation is given by

$$\begin{aligned}\phi_{\mathrm{P}}^{N+1} = \phi_{\mathrm{P}}^N + \{ &- C_{\mathrm{e}}[\tfrac{1}{2}(\phi_{\mathrm{P}} + \phi_{\mathrm{E}}) - \tfrac{1}{2}C_{\mathrm{e}}(\phi_{\mathrm{E}} - \phi_{\mathrm{P}}) \\ &- (\tfrac{1}{6} - \gamma_1 - \tfrac{1}{6}C_{\mathrm{e}}^2)(\phi_{\mathrm{E}} - 2\phi_{\mathrm{P}} + \phi_{\mathrm{W}})] \\ &+ C_{\mathrm{W}}[\tfrac{1}{2}(\phi_{\mathrm{P}} + \phi_{\mathrm{W}}) - \tfrac{1}{2}C_{\mathrm{W}}(\phi_{\mathrm{P}} - \phi_{\mathrm{W}}) \\ &- (\tfrac{1}{6} - \gamma_1 - \tfrac{1}{6}C_{\mathrm{W}}^2)(\phi_{\mathrm{WW}} - 2\phi_{\mathrm{W}} + \phi_{\mathrm{P}})] \\ &- C_{\mathrm{N}}[\tfrac{1}{2}(\phi_{\mathrm{P}} + \phi_{\mathrm{N}}) - \tfrac{1}{2}C_n(\phi_{\mathrm{N}} - \phi_{\mathrm{P}}) \\ &- (\tfrac{1}{6} - \gamma_2 - \tfrac{1}{6}C_{\mathrm{N}}^2)(\phi_{\mathrm{N}} - 2\phi_{\mathrm{P}} + \phi_{\mathrm{S}})]\end{aligned}$$

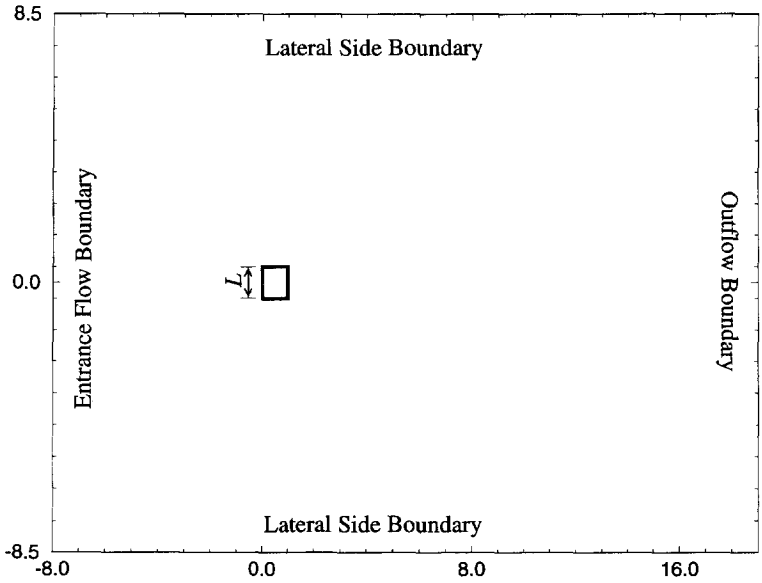

Fig. 1. Schematic of the computational domain.

$$+ C_S[\tfrac{1}{2}(\phi_P + \phi_S) - \tfrac{1}{2}C_S(\phi_P - \phi_S)$$

$$- (\tfrac{1}{6} - \gamma_2 - \tfrac{1}{6}C_S^2)(\phi_P - 2\phi_S + \phi_{SS})]$$

$$+ \gamma_1(\phi_E - 2\phi_P + \phi_W) + \gamma_2(\phi_N - 2\phi_P + \phi_S) + s_P\Delta t\}^N, \tag{15}$$

where P denotes the present point, W denotes the point west of the present point, or left in the x_1 direction, WW denotes the point farther west. Accordingly, the subscripts E, N and S may be interpreted in a similar fashion. C_e is the Courant number on the east of the present point, i.e., $C_e = u_e \Delta t/\Delta x_1$. $\gamma_1 = (\nu + \nu_{SGS})\Delta t/\Delta x_1^2$ and $\gamma_2 = (\nu + \nu_{SGS})\,\Delta t/\Delta x_2^2$. Here ν_{SGS} is the subgrid viscosity, which is calculated using Eq. (3). The pressure field is solved with a successive overrelaxation method as used by Hirt et al. [22]. This procedure ensures that the flow field is divergence free.

The computational domain, with a uniform grid of size $0.1L$, is $27L$ in the stream-wise direction and $17L$ in the cross-stream direction (see Fig. 1). The prism is located at the center in the lateral direction, and its front face is at a distance of $8L$ from the entrance flow boundary.

The computations were carried primarily on the computer facilities at the University of Notre Dame. A flow simulation at a Reynolds number about 10^5 requires about 5 hours of user time on an IBM SP1 computer, or about 6.5 hours on a Sun Spare 20 workstation, to march for a non-dimensional time of 100 which is equal to about 14 lift force oscillation cycles.

2.3. Implementation of boundary conditions

The boundary condition for the velocity at the domain entrance is specified to be equal to the far-field uniform flow, with a unit velocity in the x_1 direction and a zero component in the x_2 direction. On the two lateral side boundaries, either far-field uniform velocity or a free boundary condition, $\partial/\partial n = 0$, can be used, and no significant difference was noted between the results obtained from these boundary conditions.

The outflow boundary condition is specified using the Sommerfeld radiation condition, as used by Halpern and Schatzman [23],

$$\frac{\partial \bar{u}_i}{\partial t} + U_0 \frac{\partial \bar{u}_i}{\partial x} = 0. \tag{16}$$

Nakamura et al. [24] discussed various outflow boundary conditions and found that this condition performed much better than the free boundary condition $\partial/\partial n = 0$, and other conditions he examined. The current study also found that this condition results in a minimum boundary reflection and does not lead to divergence even for high Reynolds numbers. The free outflow condition $\partial/\partial n = 0$ was also tested and found to cause numerical instability for Reynolds numbers greater than 100. Except for cases with very low Reynolds numbers, the use of free boundary condition at the outflow boundary resulted in vortices formed near the outflow boundary, as well as zones of high pressure which subsequently influenced the entire flow field leading to a numerical instability.

The no-slip and no-penetration boundary conditions are used on the solid walls. To implement these, it is necessary to use some fictitious points inside the solid wall boundaries. A quadratic interpolation is used to specify these points and is found to give slightly better results than the conventional approach discussed in computational fluid dynamics texts [25, 26].

For points on the corners of the solid walls, it is not possible to apply the interpolation in the same way as other locations, thus other interpolation schemes are used. One such interpolation scheme, proposed by Davis and Moore [20], when applied, manifests a distinct discontinuity in the time-averaged pressure distribution at the front corners. The details are discussed later. Several other interpolations are examined here, all of which exhibited similar pressure discontinuity perhaps due to the flow field characteristics which result in numerical error. Previous numerical simulations have not closely examined this phenomenon.

3. Simulation results and discussion

3.1. Velocity field

Time histories of the velocity and pressure field are generated using the method described above, with a computed potential flow for the same configuration or the output from a previous simulation serving as the initial flow field setup. In either case,

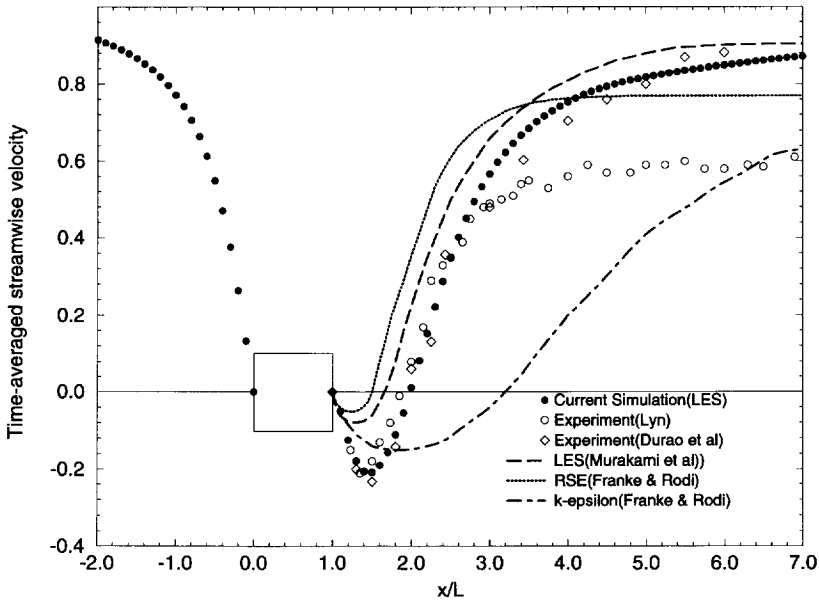

Fig. 2. Time-averaged streamwise velocity along the symmetry line.

the vortex-shedding process (for $Re = 10^5$) begins without requiring any initial disturbance. The time-averaged streamwise velocity on the symmetry line is reported in Fig. 2, together with the experimental results by Lyn [27] and Durao et al. [28], and the numerical results by Sakamoto et al. [13,15,16] and Franke and Rodi [2]. Upstream of the square, only the current simulation results are presented since the difference among the various studies presented is extremely small. In the wake flow, the current simulation results show a very good agreement with the experimental results. It should be noticed that the three-dimensional results by Sakamoto et al. deviate from the current simulation results, although both are based on LES modeling. The discrepancy may be due to the numerical methods and boundary conditions specified in this study rather than the turbulence model itself. It may also be argued the difference may be due to the fact that the Sakamoto et al. simulation was three-dimensional while the current simulation is two-dimensional. The comparison will be more evident in the pressure distribution results. Indeed, different turbulence models do influence the results as the differences among the results of $k-\varepsilon$, RSE and LES in Fig. 2 clearly demonstrate this.

The velocity fluctuation history, as in a typical wind tunnel study, are recorded at two points, A and B (Fig. 3). Fig. 4 shows the power spectrum of the u_1 velocity fluctuation at positions A and B. It can be seen that the velocity fluctuations at A are distributed over a narrower frequency range than those at point B, reflecting flow characteristics of their respective location.

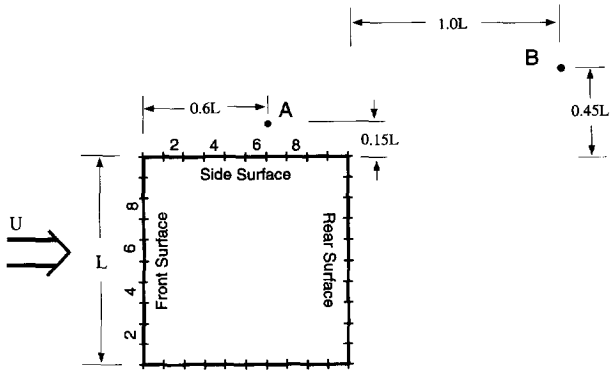

Fig. 3. Location of sampled points of interest.

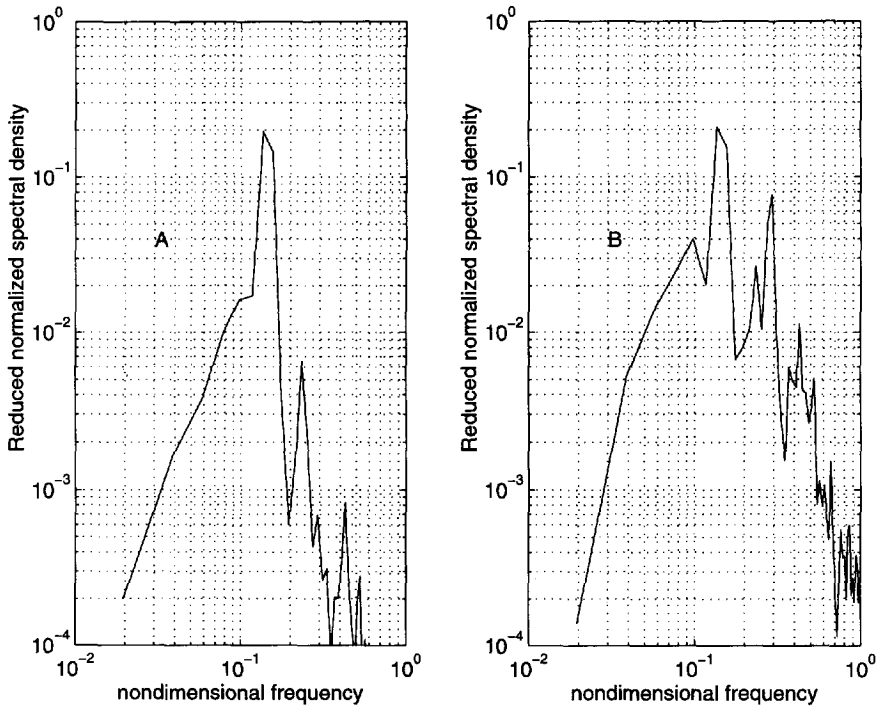

Fig. 4. Power spectra of streamwise velocity u_1 at A and B.

3.2. *Pressure field*

3.2.1. *Mean pressure distribution on the square prism*

Fig. 5 shows the distribution of the mean pressure coefficients, defined as $\bar{p}/(\frac{1}{2}\rho U_0^2)$, on the surface of a square prism. The front side facing the oncoming flow exhibits

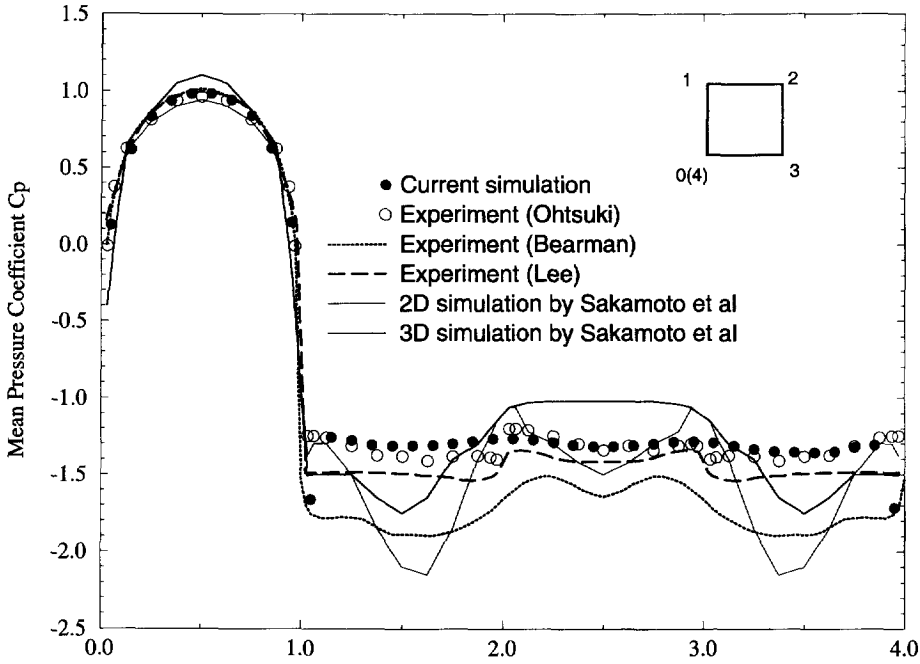

Fig. 5. Distribution of the mean pressure coefficient.

a stagnation face pressure field, whereas the side and back face show a separated region pressure field. In comparison with the experimental data [29–31] and the simulation results of Sakamoto et al. [15], the current simulation results clearly compare more closely to the experimental data, except at two points at the corners of the front face. The 2D results of Sakamoto et al. [15] are quite different from the experimental results, especially in the negative pressure regions. For example, on the two side surfaces of the square, the 2D results show that the pressure coefficient can be as low as -2.0, while the experimental value is around -1.4. The team's 3D results are better, but still exhibit a significant deviation from the experimental data in the regions of negative pressure. This is especially evident in the 3D results for the leeward face, which show the pressure coefficient to be around -1.02, as compared to the experimental value of near -1.3. As mentioned earlier concerning the results of the centerline velocity, the discrepancies between the current simulation and the results by Sakamoto et al. [15] may not be due to the turbulence model, since both used LES, but may instead be a result of the numerical method or boundary condition specifications. For example, the treatment of the outflow boundary by a free boundary condition ($\partial/\partial n = 0$) may introduce errors in the simulated results. As noted earlier, a convective boundary condition provides a more realistic condition.

In this study, it is noted that the pressure coefficients at the two points exactly at the two upwind corners deviate from the expected trend; however, their values remain

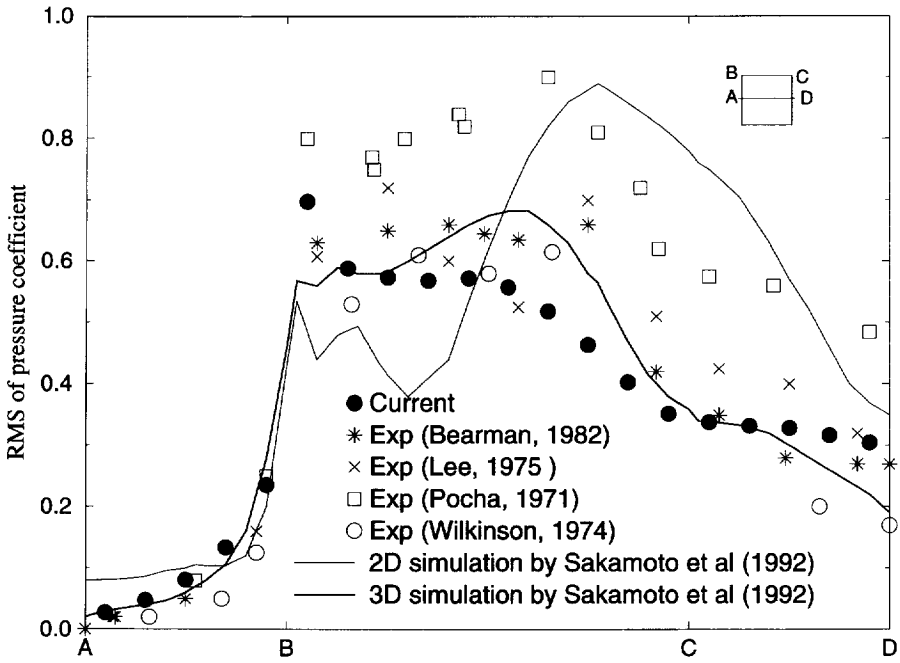

Fig. 6. Distribution of the RMS of pressure fluctuation.

close to the measured values when compared to the overall deviation present in other reported numerical results. This peculiar result was first suspected to be due to the half grid space associated with these points. Accordingly, several special schemes were designed to improve the predictions, yet this trend persisted irrespective of the numerical scheme for Reynolds numbers sufficient to produce vortex shedding. It is also observed that when the Reynolds number is low enough to prevent vortex shedding, i.e. less than 60, the pressure discontinuity disappears.

3.2.2. RMS pressure

In Fig. 6, the root mean square (RMS) values of the pressure fluctuations on the surface of the square prism are presented. The lowest RMS is at the center of the front surface, while higher values of pressure fluctuations appear on the two side faces. On the rear side, the fluctuations decrease as the centreline on the back face is approached. Again, numerical results are compared with the available experimental results and are found to be in good agreement. The range of Reynolds numbers in the cited references in Fig. 6 are listed here: Bearman and Obasaju ($Re = 2 \times 10^4$) [30], Lee ($Re = 1.76 \times 10^5$) [31], Pocha ($Re = 9.2 \times 10^4$) [32], and Wilkinson ($Re = 10^4$–10^5) [33]. Note that the 3D results of Sakamoto et al. [15] are also very close to the experimental results, while their 2D results differ substantially.

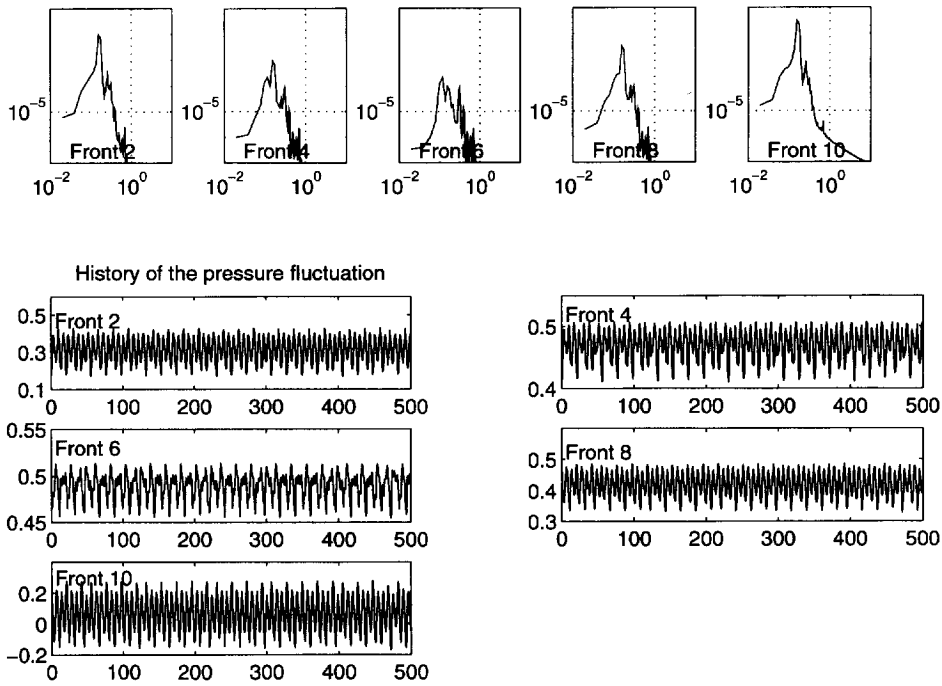

Fig. 7. Reduced normalized power spectra and time histories of pressure on front surface of the prism.

3.2.3. Power spectra of pressure and force

Figs. 7–9 show the power spectra and the time histories of the pressure fluctuations at various locations around the surface of the prism. Each side of the square prism is divided into 10 segments, and the pressure at five points corresponding to the 2nd, 4th, 6th, 8th, and 10th points are recorded. Fig. 7 describes the spectra and time histories of the pressure on the front face. Observe that the bandwidth of the power spectrum at a point is a function of its location on the surface. The locations closer to the stagnation point tend to be broad-banded, reflecting the fluctuations in the approach flow according to strip and quasi-steady theories, whereas near the side face, the spectral contents exhibit narrow banded characteristics, reflecting the influence of the wake. The time history plots of the pressure fluctuations also depict a similar trend. Moving toward the side faces (Fig. 8), one observes the spectral contents become narrow banded, reflecting the dominance of narrow banded fluctuations due to vortex shedding. Fig. 9 shows the spectrum and time histories of pressure on the rear side, which confirm that the spectrum have a wider bandwidth than those on the side faces. On the leeward face, the time histories indicate a wider range of frequencies, which is portrayed by the relatively broad banded spectral contents.

The lift and drag forces are the synthesis of pressure fluctuations on the two lateral sides and front and back faces, respectively. Clearly, the spectra of the lift force reflect the side face pressure spectra. Likewise, the drag force spectrum portrays the spectral characteristics of pressure fluctuations on the front and back faces.

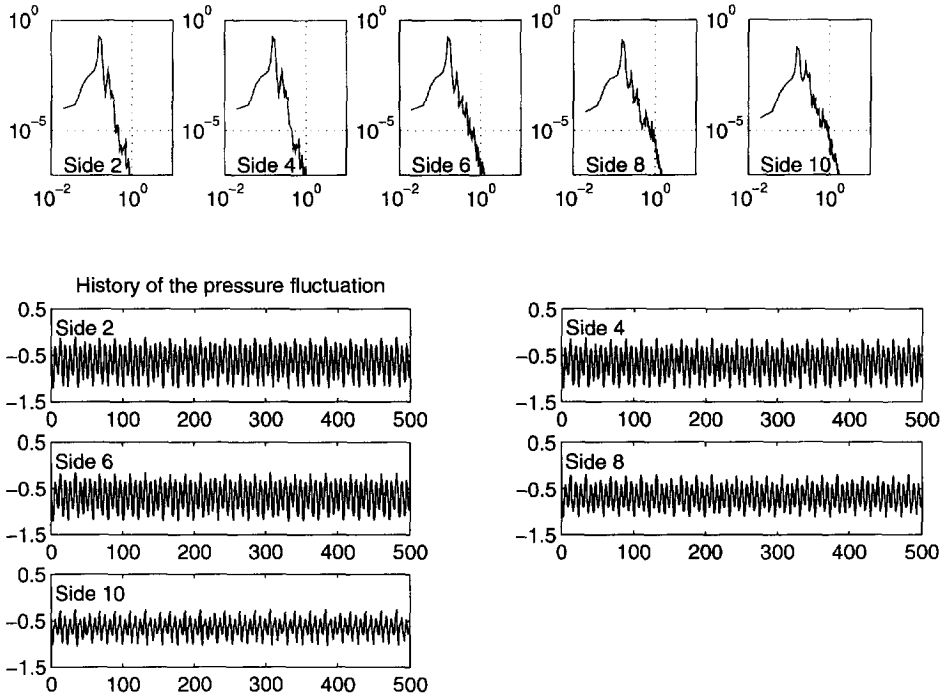

Fig. 8. Reduced normalized power spectra and time histories of pressure on the side surface of the prism.

In Fig. 10, the power spectra of lift and drag force on the square prism are presented. The lift force spectrum is characterized by a peak, at approximately 0.14, which is the Strouhal number. The drag force coefficient indicates a bi-modal spectrum, in which the dominant peak is twice the Strouhal number. Upon comparison of these results with the experimental findings [34], it is concluded that while the numerical results are close qualitatively, they do not correspond with the experimental data to the same degree as noted for the mean and RMS pressure coefficients.

The average value of the lift coefficient is zero, as the symmetry of the flow field suggests, with a lift force coefficient standard deviation of 1.06. The mean value of drag force coefficient is 2.01, and its standard deviation is 0.21. In Table 1, a comparison with reported experimental results under uniform or smooth approaching flow is made, in which the Strouhal number from the simulation is in good comparison with the experimental data. Since the RMS lift and drag coefficients and their spectral descriptions are sensitive to approach flow characteristics, the current results are in better agreement with Lee's experiments conducted in the smooth approach flow.

3.2.4. Pressure correlation

The numerically simulated data is utilized to examine the chordwise cross correlation structure of the pressure field. A total of 40 locations around the periphery of the

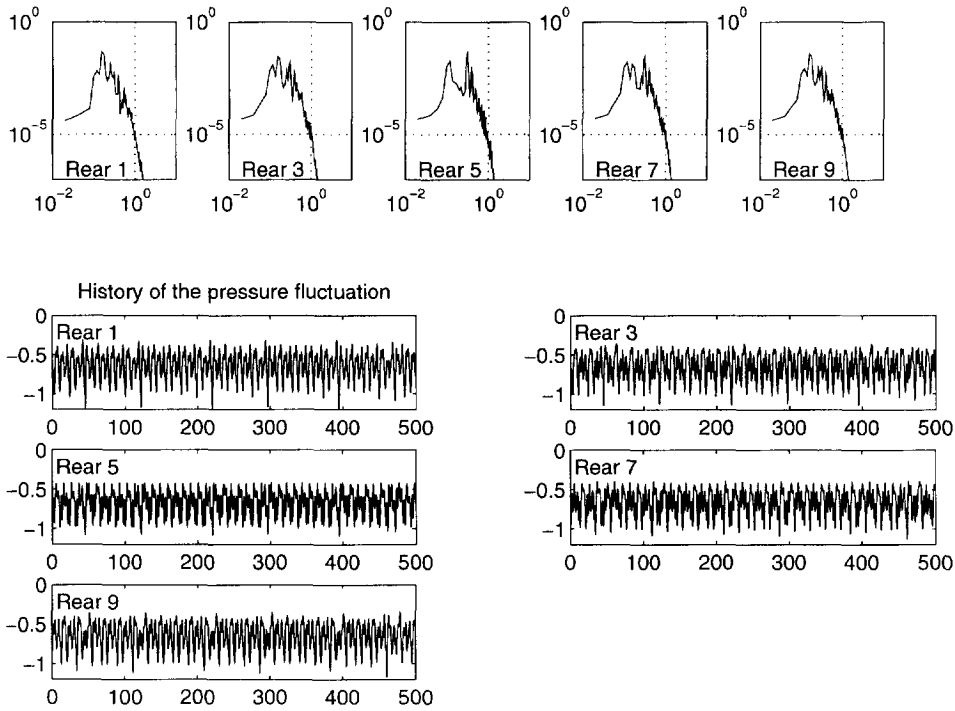

Fig. 9. Reduced normalized power spectra and time histories of pressure on the rear surface of the prism.

prism were sampled, as indicated in Fig. 3. The cross-correlation coefficient is defined as R_{ab}, where subscript 'a' represents the reference location and 'b' is the location of the second point. In Fig. 11, R_{ab} is plotted for seven different locations of the reference location, a, and b is varied to include each of the 40 sampled locations. It is noted that the correlation is sensitive to the reference location, suggesting a non-homogeneous nature of the pressure field. It was also observed that the correlation with respect to point 6 on the stagnation face exhibits a very low value with respect to all other locations. Depending upon the reference location, the correlation structure remains uniform over the separated regions of the side faces, whereas the front and rear faces are characterized by sharply increasing or decreasing correlation. These points at the dominant presence of an antisymmetric correlation pattern associated with vortex shedding. In a later section, this correlation pattern is corroborated by streakline plots. Furthermore, the numerical results are compared with an experimental study by Lee [31] in Fig. 12, where the chordwise correlation coefficients with reference to a point on the side surface, as indicated in the figure, are plotted. The agreement is very good.

3.2.5. Eigenfunction analysis of pressure fluctuation

After the fluctuating pressure around the circumference of the square prism is decomposed into its orthonormal eigenfunctions [31,37–39], a pressure time history

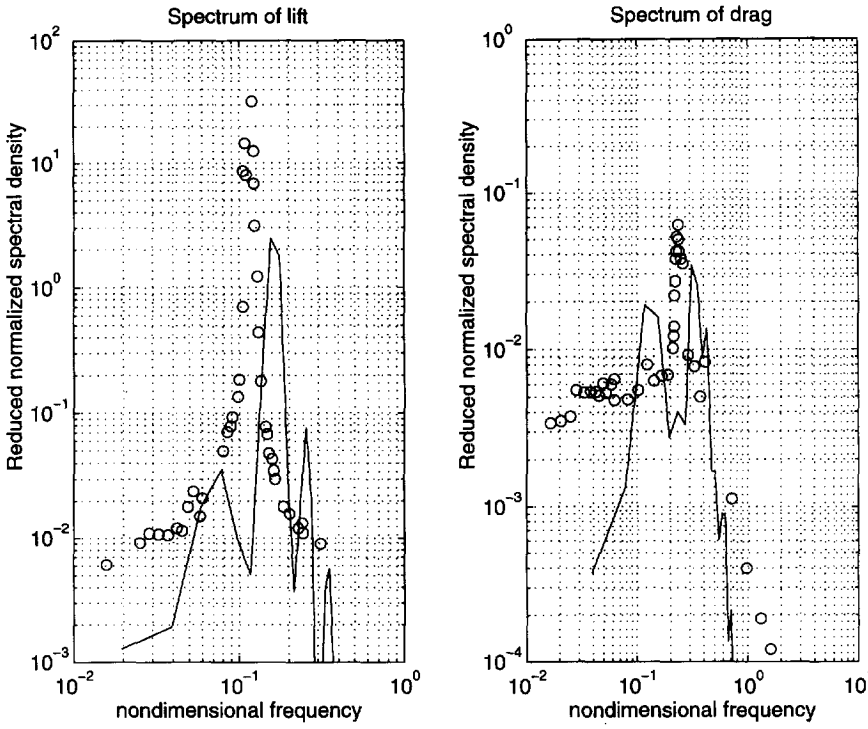

Fig. 10. Power spectra of lift and drag (——, numerical; ○, experimental).

Table 1
Comparison of mean and RMS of C_L and C_D and Strouhal number with experiments

	RMS of C_L	Mean of C_D	RMS of C_D	St. number
Current simulation	1.06	2.01	0.21	0.14
Vickery, 1	1.32		0.17	0.12
Vickery, 2	1.27		0.17	
Lee	1.22	2.05	0.22	
Bearman and Obasaju [30]	1.2			0.13
Nakamura and Mizota [35]	1.0			
Okajima [36]				0.13

may be expanded in optimal orthogonal functions, following Mercier's Theorem and the Karhunen–Loeve expansion,

$$P(x,t) = \sum_{n=1}^{N} a_n(t)\Phi_n(x), \tag{17}$$

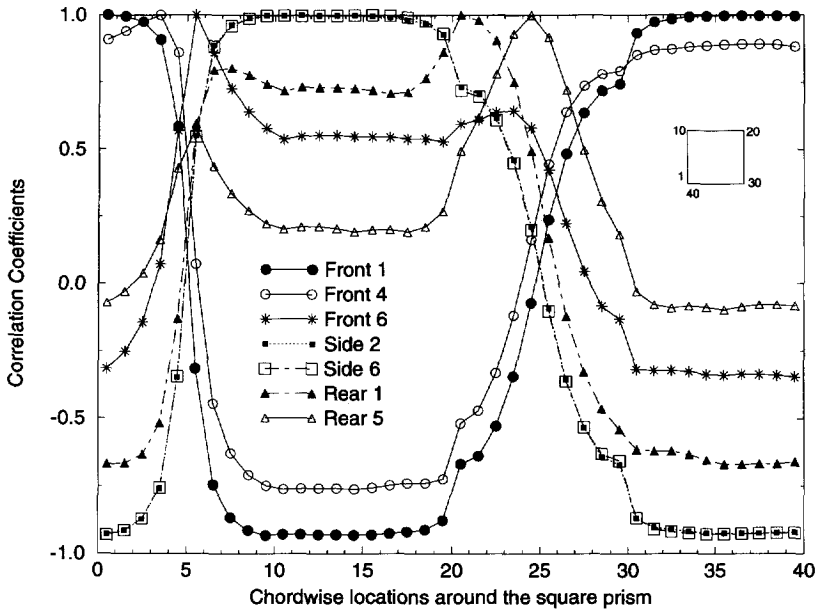

Fig. 11. Chordwise correlation coefficients of pressure fluctuation.

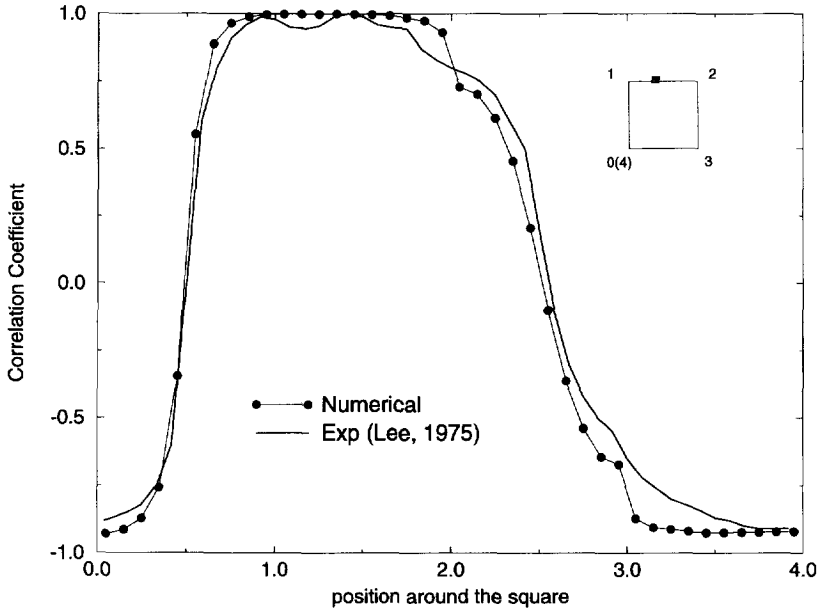

Fig. 12. Comparison of chordwise correlation with experiment.

Table 2
Eigenvalues and corresponding energy containment

	% 1st eigenvalue	% 2nd eigenvalue	% 3rd eigenvalue	% 4th eigenvalue	% 5th eigenvalue	% total of first 5 eigenvalue
Current Simulation	74.0	16.1	3.8	3.3	1.3	98.0
Experiment (Lee, 1975)	79.7	7.3	3.8	2.3	1.7	94.8

in which

$$\overline{a_n(t)a_m(t)} = \delta_{nm} \int_0^L \phi_n(x)\phi_m(x)\,\mathrm{d}x = \lambda_n \delta_{nm}, \quad 0 \leqslant x \leqslant L.$$

In the preceding equation, δ_{nm} denotes the Kronecker delta function, $\phi_n(x)$ and λ_n represent the eigenfunction and the associated eigenvalue, respectively. The orthogonal eigenfunctions are obtained by decomposing the pressure covariance as follows:

$$\int_0^L R(x_1, x_2)\,\mathrm{d}x_2 = \lambda_n \phi_n(x_1). \tag{18}$$

For a discretely sampled random pressure field $p(x, t)$ between interval 0 and L at K locations, with a separation distance of Δx, the preceding integral equation reduces to

$$\Delta x \sum_{h=1}^{K} R(x_g, x_h)\,\phi_n(x_h) = \lambda_n \phi_n(x_g), \quad g = 1, \ldots, K. \tag{19}$$

It can be shown that the integral of the mean square pressure fluctuations over the surface is equal to the sum of the eigenvalues, with each eigenvalue representing the energy contained in its associated spatial eigenfunction. Each eigenfunction may then be assigned physical significance on the basis of its spatial variation. For example, a symmetrical eigenfunction may result from the large-scale incident turbulence, whereas an antisymmetric eigenfunction may result from vortex shedding, the lateral component of turbulence, or fluctuating separation points. Note that the orthogonality condition is satisfied by both the symmetric and antisymmetric spatial distribution of the functions.

The covariance matrix of the chordwise pressure fluctuations was analyzed to obtain the eigenvalues and eigenfunctions, with the results showing that the first five modes contained 98% of the total energy. The percentage of energy contained in the first five modes are, respectively, 74.0%, 16.1%, 3.8%, 3.3% and 1.3%, which are also listed in Table 2 and compared with the wind tunnel results of Lee for a uniform approach flow. The total energy of the first five eigenvalues in the simulation is slightly

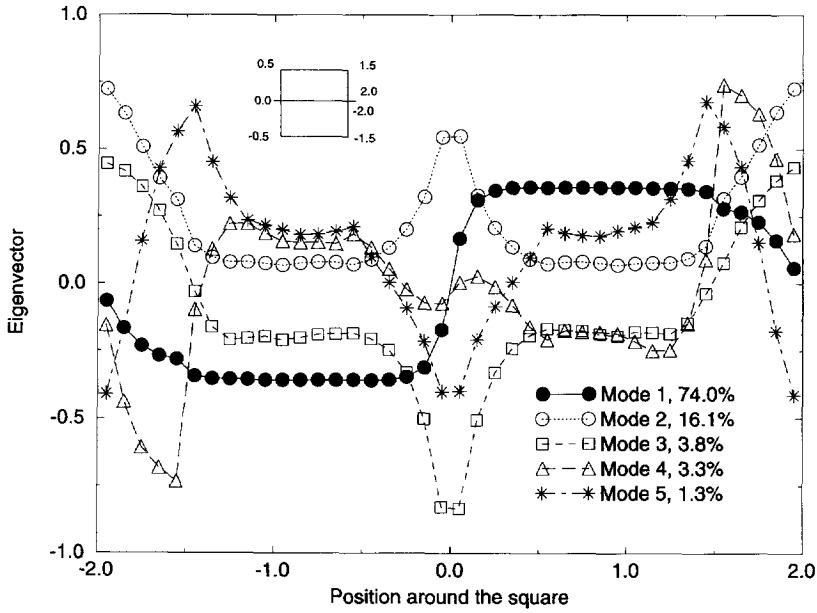

Fig. 13. First five eigenvectors representing the pressure field around the square prism.

higher than the experimental findings, which may be due to slight variations in the approach flow.

The eigenfunctions corresponding to the first five eigenvalues are plotted in Fig. 13. The main mode of the simulation is plotted in Fig. 14 together with the experimental result of Sakomoto et al. [31]. The values of the experimental data are directly taken from Lee's paper, but the numerical values are renormalized for consistency. The comparison of Lee's findings and those of this study exhibit generally good agreement, with the exception of the front face. Some of this could be attributed to a higher number of observations on each face in this study as compared to the experimental measurements. It is observed that 74.0% of the total energy is in the first antisymmetric mode. Also, the fourth mode is antisymmetric and contains 3.3% of the total energy. The second mode is symmetric, which may reflect the incident uniform flow or a very large-scale flow structure. The third and fifth modes are again symmetric, but contain much less energy than the second mode. They may represent some structure less than the second mode, but comparable in size to the square prism.

3.2.6. Probability distribution of pressure fluctuation

The probability distribution of pressure fluctuation is an important quantity from design considerations. A brief discussion is included in the light of the simulated data. Fig. 15 addresses the sixth point on the side face with a total number of 160 000 points sampled at a time interval of 0.025. In the top panel, a part of the time history of the

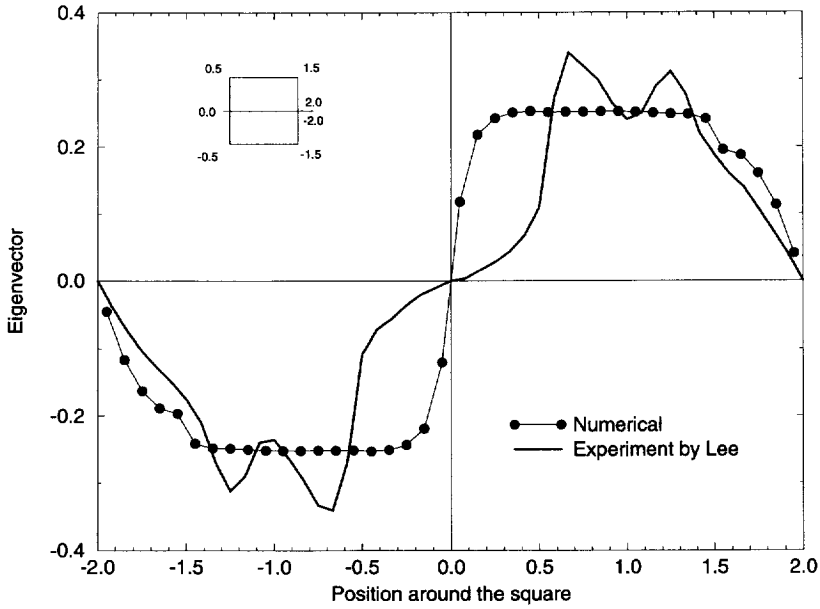

Fig. 14. Comparison of the first eigenvector with experimental result.

fluctuation is shown, which is both amplitude and frequency modulated. The associated probability density function is similar to a process represented by a sinusoidal function with added noise. Fig. 15 also shows similar results for the sixth point (just on one side of the centerline) on the front side of the square prism. Here, the pressure time history exhibits a more narrow-banded signature than that of the side face, which reflects the approach flow characteristics.

3.3. Numerical flow visualization

Fig. 16 shows a time sequence of streakline plots of the flow around a square prism. A streakline is the trace of a series of particles released at a certain position at the entrance of the flow domain. In this study, they are released at the entrance boundary, which is 8 times the side length of the square prism in front of the prism, and at a lateral span exactly corresponding to the position of the square. For every line, a new particle is released at normalized time of 0.1 and marched forward with the flow as a massless marker similar to those in the marker and cell (MAC) method. A bivariate linear interpolation in space is conducted for the particle velocities [26], and the averaged velocity based on the previous time step and the current time step is utilized. In Fig. 16, 8 frames of streaklines are presented at 8 time sequences in a complete cycle of the lift force. For every frame, the corresponding lift force is drawn on its upper left-hand side panel, in which the black dot represents the instantaneous lift force value induced by the flow field corresponding to the streamlines shown.

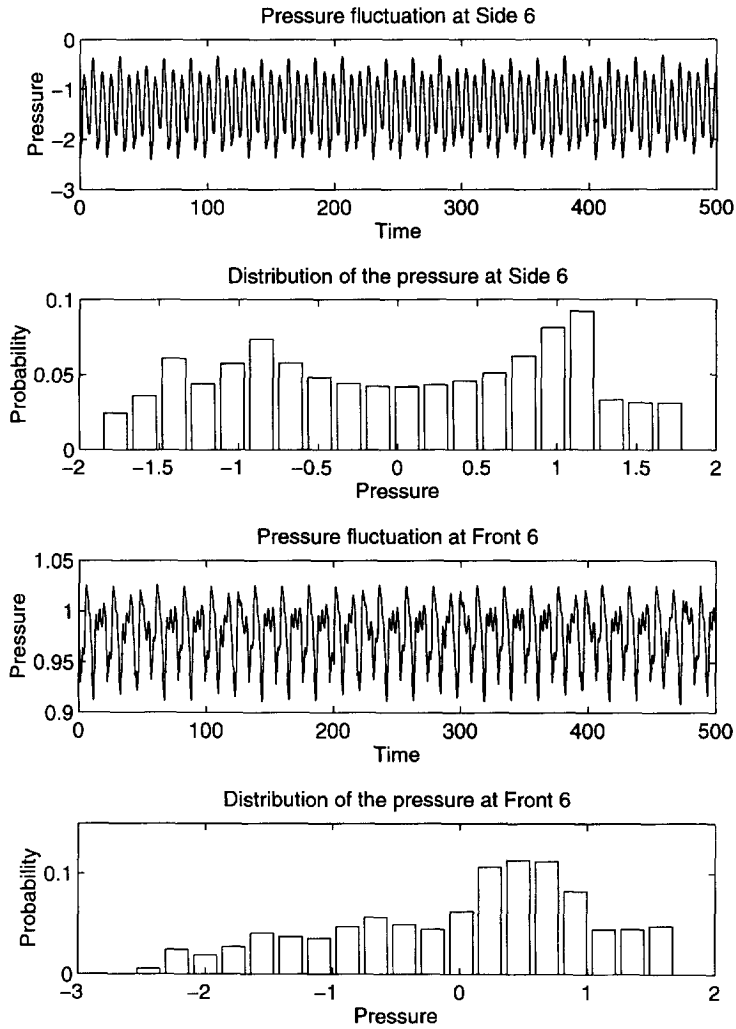

Fig. 15. Probability distribution of pressure at side and front faces.

The sequence of streaklines clearly describes the shedding of vortices from the prism. In Frame 1, the total lift force on the square is zero, and three vortices are indicated by A, B and C behind the square. A is already shed, preparing to exit out of the stream. B was originally formed from the lower side of the square and is still attached to the rear side of the square. In Frame 2, A moves further outside with the stream, and B is completely shed off the rear side surface, while C moves to the center of the rear side surface. In Frames 3 and 4, this trend continues. In Frame 5, half a cycle of the lift force is completed, and it may be concluded that the streaklines close to the square in Frame 5 are similar to those in Frame 1, but only reversed. In

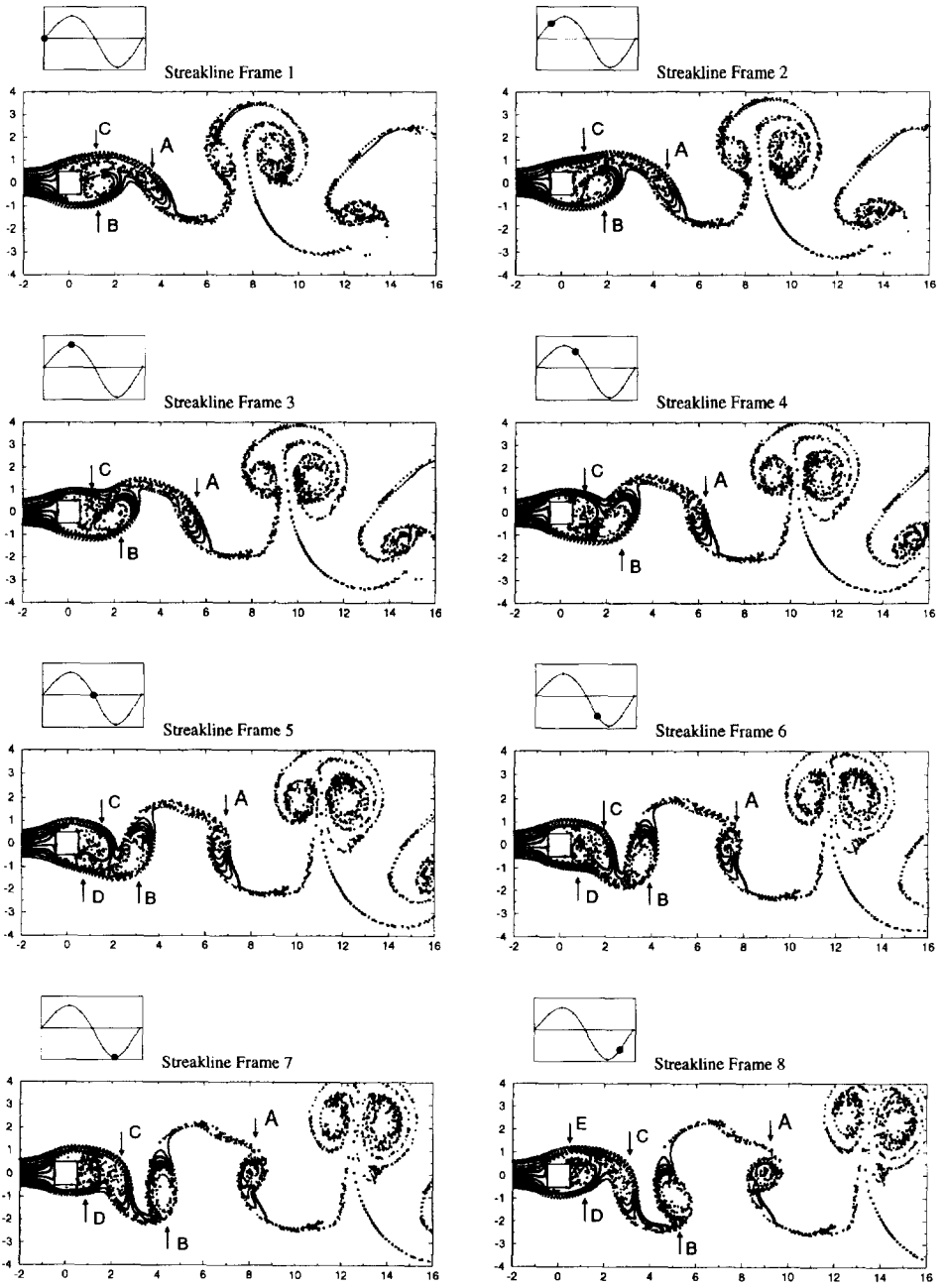

Fig. 16. Streaklines of flow around a square prism.

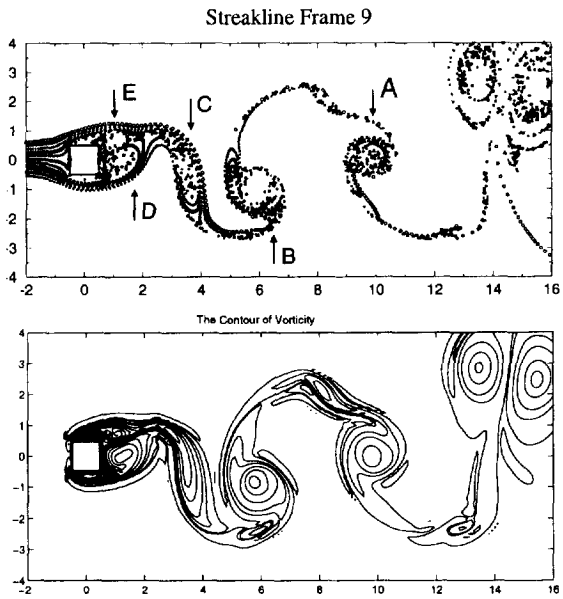

Fig. 17. Streaklines and isovorticity plots of the flow field.

Frame 5, a new vortex D is formed at the lower side behind the square. In this frame, D is in a similar position as C was in Frame 1. In Frames 5–8, genesis of vortex-shedding process is similar to that observed in Frames 1–4. In Frame 9, shown in Fig. 17, another new vortex E is formed. According to this trend, in every full cycle of the lift force, two vortices are shed, one from the lower side and one from the upper side of the square.

In Fig. 17, instant streaklines are shown in comparison with an isovorticity plot at the same instant. Note that the high-intensity vorticity contours correspond exactly with the streaklines.

3.4. Influence of aspect ratio

Fig. 18 shows the mean pressure distribution around a rectangular prism with an aspect ratio of 1:2, and a comparison with experimental results given by Miyata and Miyazaki [40], which shows a good agreement. For a 1:2 rectangular prism, the pressure on the two side faces and the rear face are higher (less negative) than those of a square prism, due to the influence of the afterbody on the separated flow. In Fig. 19, displaying mean pressure distributions over prisms with different aspect ratios confirms that with an increase in the streamwise body length, i.e., aspect ratio, there is a concomitant increase in pressure recovery. In Fig. 20, the RMS pressure fluctuations on the side surface of the rectangular prisms with different aspect ratios are compared, revealing that for a square prism and a prism of aspect ratio of 2:3, a local minimum

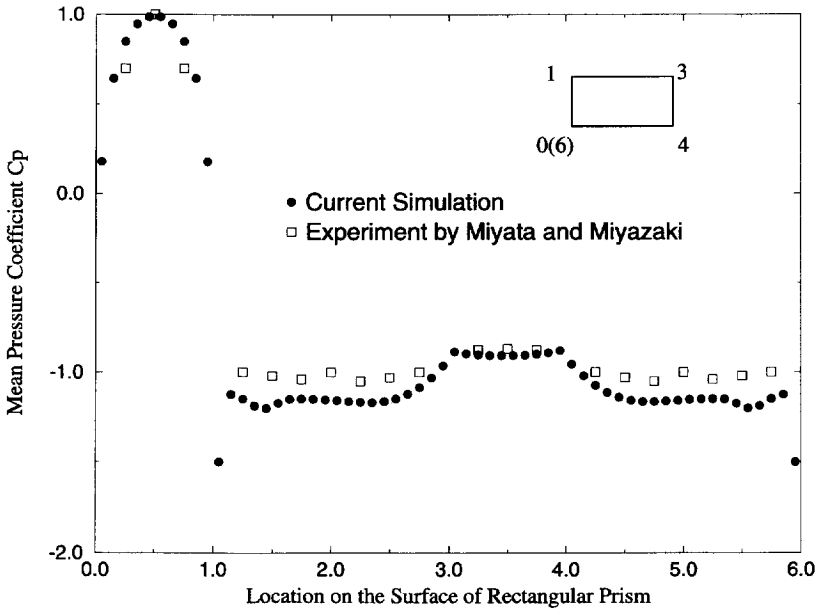

Fig. 18. Mean pressure distribution around a 1:2 rectangular prism and comparison with experiment.

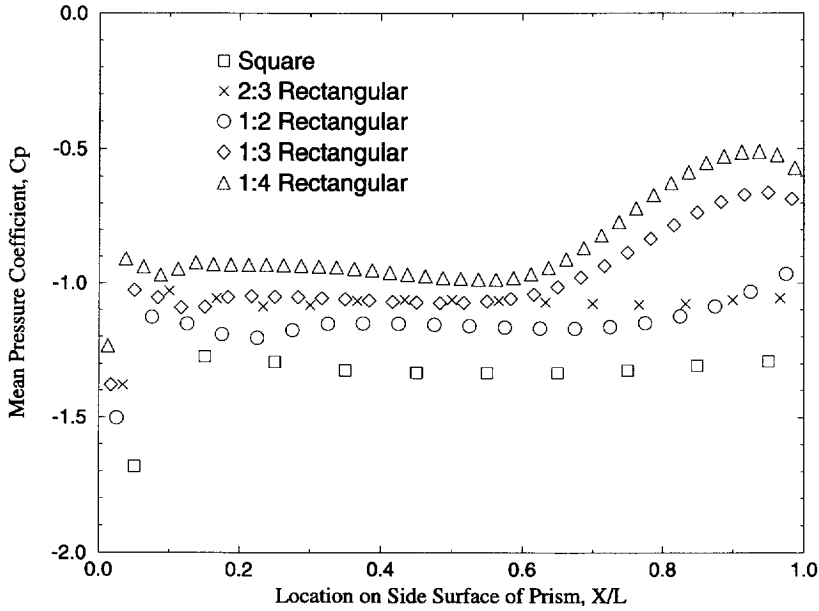

Fig. 19. Comparison of mean pressure distribution on side face of rectangular prisms with different aspect ratios.

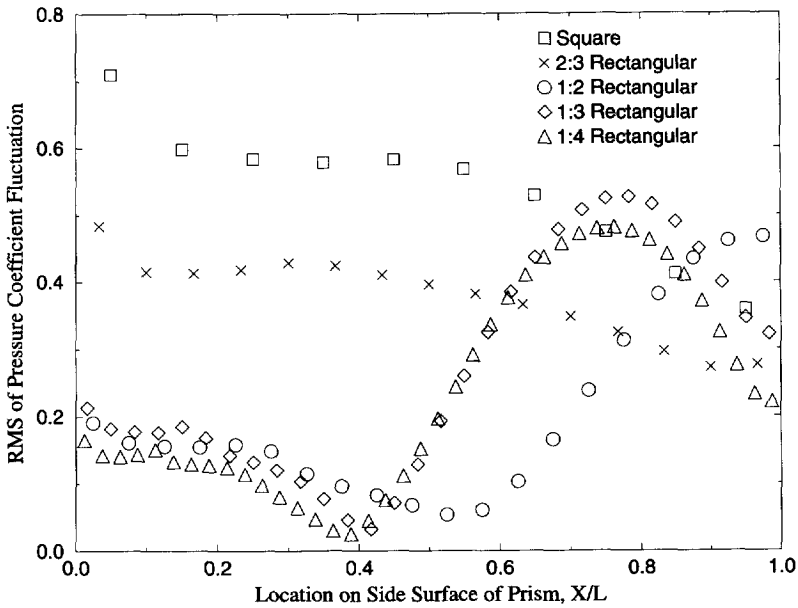

Fig. 20. Comparison of RMS of pressure fluctuations on side face of rectangular prisms with different aspect ratios.

on the side face does not exist, but for 1:3 and 1:4 rectangular prisms local minima are observed. This is due to the reattachment of the flow. It can also be noted in Fig. 19 that the mean pressure distribution on the side face of the 1:3 and 1:4 rectangular prisms exhibit a pressure increase toward the rear end, while the square and 2:3 rectangular prism do not manifest this tendency. These are indications of reattachment of the flow which leads to pressure recovery as the trailing edge of the side face is approached, and can be confirmed by the streaklines as shown in Fig. 21. The streaklines reveal that the 2:3 rectangular prism, similar to a square, does not exhibit reattachment. The 1:2 rectangular prisms show some tendency toward reattachment, while the 1:3 and 1:4 rectangular prisms experience complete reattachment. Table 3 lists the mean and RMS values of drag force and the Strouhal number for rectangular prisms with aspect ratio ranging from 2:3 to 1:4. Again, it is noted that the mean drag force decreases with an increase in the streamwise length of the body as a result of pressure recovery. This is in agreement with the results reported in Fig. 19. These values are also compared to available experimental results reported in the literature, and they are generally in good agreement.

3.5. Grid refinement study

To study the accuracy of the numerical scheme used here, a grid refinement study is conducted. Roache [43] suggested a method for reporting numerical convergence

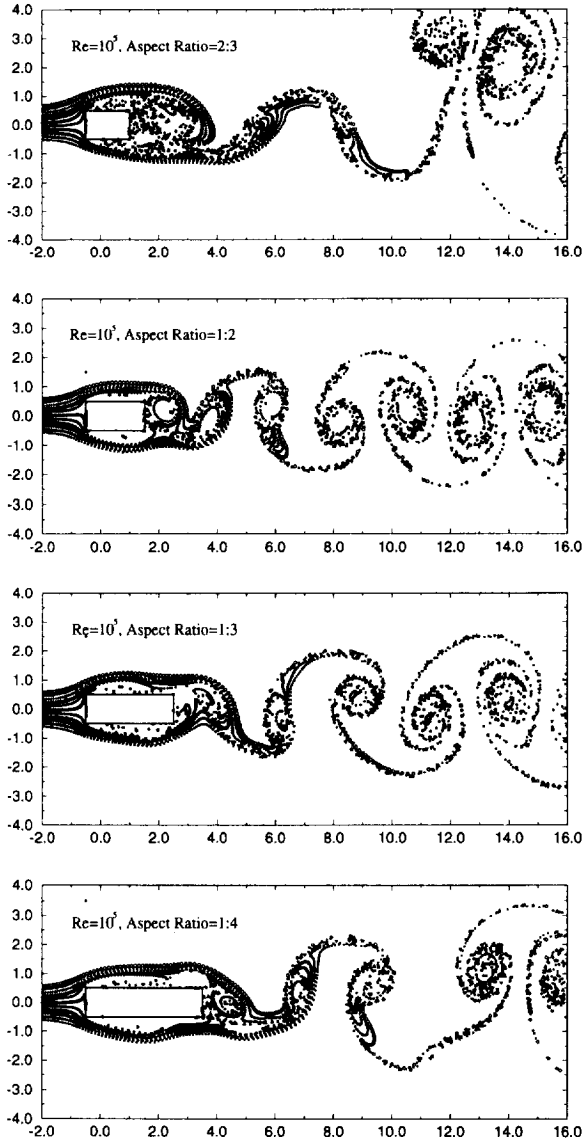

Fig. 21. Streaklines of flow around rectangular prisms of different aspect ratios.

uniformly, based on Richardson extrapolation. For the LES, there has been limited experience concerning the reporting of errors associated with grid refinement study. One way to refine LES grid is to keep the value of Δ in the Smagorinksy model invariant, while refining Dx, Dy, and Dz. The other approach involves refinement of grid uniformly, while allowing Δ to vary in each refinement since Δ is defined as

Table 3
Strouhal number and drag coefficient of rectangular prisms

Aspect ratio	2:3	1:2	1:3	1:4
Mean of C_D, Current simulation	1.72	1.62	1.56	1.43
Mean of C_D, experiment, [41]	1.8	1.6	1.4	1.4
Mean of C_D, experiment [40]		1.65		
RMS of C_D, curent simulation	0.19	0.14	0.0927	0.168
St, current simulation	0.10	0.18	0.17	0.15
St, experiment [36,42]	0.09	0.08	0.17	0.135

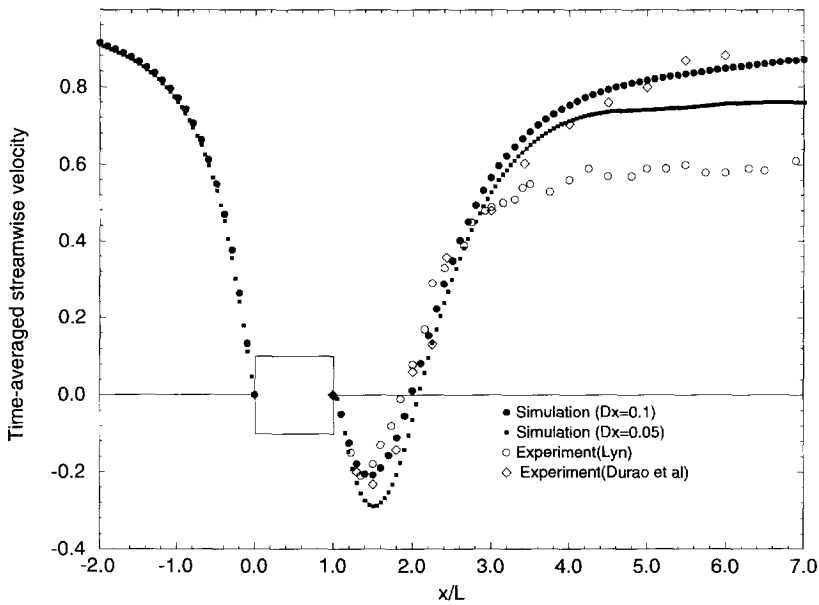

Fig. 22. Results of grid refinement for the time averaged centreline velocity distribution.

$(Dx \cdot Dy \cdot Dz)^{1/3}$ in the Smagorinsky model. Theoretically, the results should converge to the 'true solution' as the grid refines. Obviously, these two approaches are not equivalent and may not necessarily produce the same results, thus warranting additional investigation through numerical experiments.

In the simulation of turbulent channel flow using LES, Mason and Callen [44] changed the grid size, Dy, while keeping $C_s \cdot Dy$ invariant, observing substantial variation with ground changes. Though their purpose was to study the effect of C_s instead of grid refinement, the results also raised doubts regarding the influence of grid refinement on their LES-based simulation.

In this study, a grid system with half the grid size (i.e., $Dx = Dy = 0.05$) and $\Delta = 0.1$ in the Smagorinsky model was used. The results for the time-averaged velocity

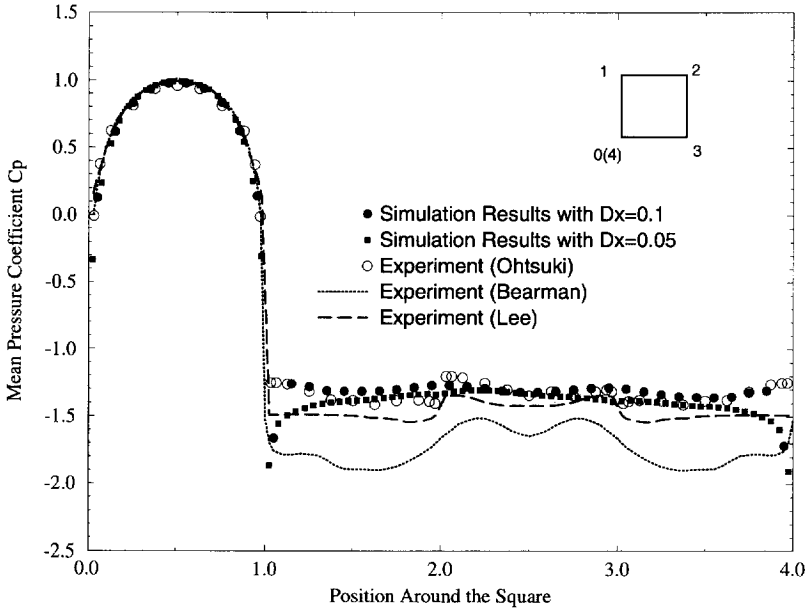

Fig. 23. Results of grid refinement for the mean pressure distribution on the square prism.

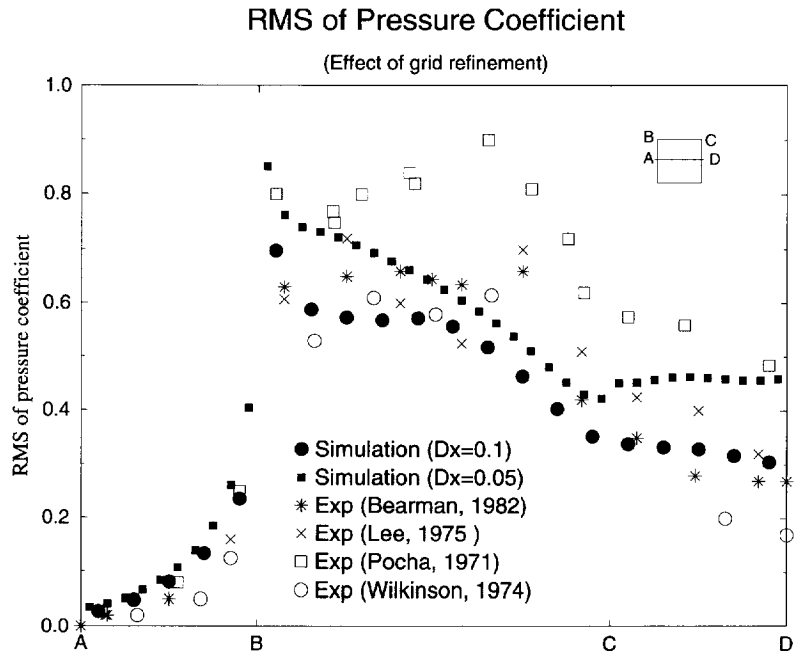

Fig. 24. Results of grid refinement for the RMS pressure coefficient distribution on the square prism.

distribution along the centerline are presented in Fig. 22, while the mean and RMS pressure distributions are presented in Figs. 23 and 24, respectively. For all these quantities, the refined grid system gives results on the front side of the square which are close to experimental findings, with some differences noted in the separated flow regions. These differences are small and repeatable and are within the range of experimental error. At the same time, these deviations are noticeable and will be further investigated and addressed in future studies.

4. Conclusions

A numerical algorithm using a staggered grid based on the QUICK scheme for the convection term, Leith's method for the temporal marching, and the LES model for the subgrid scale viscosity is presented. The LES model used here may be viewed as a coherent structure capturing technique. This scheme is utilized to compute flows around 2D prisms at a Reynolds number of 10^5.

The study computes time averaged centerline velocity distribution, mean and RMS pressure distributions around rectangular prisms and compares these results to available experimental and numerical results reported in the literature. The findings of the study are in excellent agreement with experimental data. In addition, the power spectra of the pressure and velocity fluctuations at various points of interest and their probability distributions are reported.

The chordwise cross correlation of pressure at different points on the prism is obtained which shows a good agreement with the wind tunnel results. Furthermore, an eigenfunction analysis is conducted by expanding the pressure covariance matrix. The derived eigenfunctions match well with the experimental results.

The streaklines generated in the study provide a good illustration of the vortical structure of the flow field and flow separation–reattachment characteristics of rectangular prisms with different aspect ratios. The streaklines suggest qualitative patterns of pressure distribution along side faces which corroborate with the simulated pressure distribution around prisms. Finally, a grid refinement study is conducted, and the results of the refined grid for time-averaged velocity on the centerline and the distribution of mean and RMS pressure coefficients on the square prism are presented. It is observed that the pressure on the upstream face of the square remains unchanged with grid refinement examined here, while in the separated regions there are some differences. The simulated pressure field characteristics are nonetheless very close to the experimental results.

Acknowledgements

This study was partially supported by ONR Grant No. 00041-93-1-0761 and NSF Grant Nos. CMS-9503779 and NCSA-BCS960002N. The computation was conducted partially on the SGI Power Challenge Array at the National Center for Supercomputing Applications at the Univ. of Illinois at Urbana-Champaign, and the HPCC

system at Univ. of Notre Dame. The first author was partially supported by a fellowship from the Center for Applied Mathematics, University of Notre Dame. The second author would like to acknowledge a senior fellowship from the University of Tokyo and many useful discussions with Dr. S. Murakami and his colleagues which facilitated the work reported here. The authors would also like to thank Drs. Samuel Paolucci and Joannes Westerink from Notre Dame for useful discussions.

References

[1] S. Murakami, A. Mochida and Y. Hayashi, Examining the k–ε model by means of wind tunnel test and large-eddy simulation of the turbulence structure around a cube, J. Wind Eng. Ind. Aerodyn. 35 (1990) 87–100.

[2] R. Franke and W. Rodi, Calculation of vortex shedding past a square cylinder with various turbulence models, in: Proc. 8th Symp. on Turbulent Shear Flows (1991) p. 189.

[3] V. Przulj and B.A. Younis, Some aspects of the prediction of Turbulent Vortex Shedding from Bluff Bodies, FED-Vol. 149 (ASME, New York, 1993) p. 75.

[4] W. Rodi, On the simulation of turbulent flow past bluff bodies, J. Wind Eng. Ind. Aerodyn. 46/47 (1993) 3–19.

[5] J. Ferziger, Simulation of complex turbulent flows: recent advances and prospects in wind engineering, J. Wind Eng. Ind. Aerodyn. 46 & 47 (1993) 195–212.

[6] T.S. Smagorinsky, General circulation experiment with primitive equations: Part I, basic experiments, Monthly Weather Rev. 91 (1963) 99–164.

[7] A. Pinelli and C. Benocci, Large eddy simulation of a fully turbulent plane channel flow, Technical Note 171, von Karman Institute for Fluid Dynamics (1989).

[8] J.P. Boris, F.F. Grinstein, E.S. Oran and R.L. Kolbe, New insights into large eddy simulation, Fluid Dyn. Res. 10 (1992) 199–228.

[9] P.J. Mason, Large-eddy simulation: a critical review of the technique, Q. J. R Meteorol. Soc. 120 (1994) 1–26.

[10] M. Lesieur and O. Metais, New trends in large-eddy simulations of turbulence, Ann. Rev. Fluid Mech. 28 (1996) 45–82.

[11] U. Piomelli, J. Ferziger and P. Moin, New approximate boundary conditions for large eddy simulations of wall-bounded flows, Phys Fluids A 1 (1989) 1061–1068.

[12] S. Murakami, A. Mochida and H. Kazuki, Three-dimensional numerical simulation of air flow around a cubic model by means of large eddy simulation, J. Wind Eng. Ind. Aerodyn. 25 (1987) 291–305.

[13] S. Sakamoto, S. Murakami, S. Kato and A. Mochida, Numerical study on flow past 2D square cylinder by large eddy simulation: comparison between 2D and 3D computations, Proc. 2nd Int. Coll on Bluff Body Aerodynamics and Applications, Melbourne, Australia, 7–10 December (1992) pp. 112–119.

[14] S. Sakamoto, S. Murakami, S. Kato and A. Mochida, Unsteady pressure field around oscillating prism predicted by LES, J. Wind Eng. 52 (1992) 368–373.

[15] S. Sakamoto, S. Murakami and A. Mochida, Numerical study on flow past 2D square cylinder by large eddy simulation: comparison between 2D and 3D computations. J. Wind Eng. Ind. Aerodyn. 50 (1993) 61–68.

[16] S. Murakami and A. Mochida, On turbulent vortex shedding flow past 2D square cylinder predicted by CFD, J. Wind Eng. Ind. Aerodyn. 54/55 (1995) 191–211.

[17] S. Murakami, A. Mochida and S. Sakamoto, CFD analysis of windstructure interaction for oscillation square cylinder, Wind Engineering: Retrospect and Prospect, Papers for 9th Int. Conf., New Delhi, India (1995) pp. 671–682.

[18] B.P. Leonard, A stable and accurate convective modelling procedure based on quadratic upstream interpolation, Comput. Methods Appl. Mech. Eng. 19 (1979) 59–98.

[19] F.H. Harlow and J.E. Welch, Numerical calculation of time-dependent viscous incompressible flow of fluid with free surface, Phys. Fluids 8 (1965) 2182–2189.
[20] R.W. Davis and E.F. Moore, A numerical study of vortex shedding from rectangles, J. Fluid Mech. 116 (1982) 475–506.
[21] R.W. Davis, E.F. Moore and L.P. Purtell, A numerical–experimental study of confined flow around rectangular cylinders, Phys. Fluids 27 (1984) 46–59.
[22] C.W. Hirt, B.D. Nichols and N.C. Romero, SOLA – a numerical solution algorithm for transient fluid flows, Los Alamos Scientific Laboratory Rep. LA-5852 (1975).
[23] L. Halpern and M. Schatzman, Artificial boundary conditions for incompressible viscous flows, SIAM J. Math. Anal. 20 (1989) 308.
[24] I. Nakamura, T. Watanabe and T. Yoshida, On the numerical outflow boundary condition of the viscous flow around a square cylinder, Mem. School Eng. Nagoya Univ. 45 (1993) 105–117.
[25] C.A.J. Fletcher, Computational Techniques for Fluid Dynamics, Vol. II Spr. Computat. Phys. (Springer, Heidelberg, 1988).
[26] P.J. Roache, Computational Fluid Dynamics (Hermosa, albuquerque, 1972).
[27] D.A. Lyn, Phase-averaged turbulence measurements in the separated shear flow around square cylinder, Proc. 23rd Cong. Int. Ass. Hydraulic Research, Ottawa, Canda, 21–25 August (1989) pp. A85–A92.
[28] D.F.G. Durao, M.V. Heitor and J.C.F. Pereira, Measurements of turbulent and periodic flows around a square cross-section cylinder, Exp. Fluids (1988) 298–304.
[29] Y. Ohtsuki, Wind tunnel experiments on aerodynamic forces and pressure distributions of rectangular cylinders in a uniform flow, Proc. 5th Symp. on Wind Effects on Structures, Tokyo, Japan (1978) 169–175.
[30] P.W. Bearman and E.D. Obasaju, An experimental study of pressure fluctuations on fixed and oscillation square-section cylinders, J. Fluid Mech. 119 (1982) 297–321.
[31] B.E. Lee, The effect of turbulence on the surface pressure field of a square prism, J. Fluid Mech. 69 (1975) 263–282.
[32] J.J. Pocha, On unsteady flow past cylinders of square cross-section, Ph.D. Thesis, Department of Aeronautics, Queen Mary College, London (1971).
[33] R.H. Wilkinson, On the vortex-induced loading on long bluff cylinders, Ph.D. Thesis, Faculty of Engineering, University of Bristol, England (1974).
[34] B.J. Vickery, Fluctuating lift and drag on a long cylinder of square cross-section in a smooth and in a turbulent stream, J. Fluid Mech. 125 (1966) 481–494.
[35] Y. Nakamura and T. Mizota, Unsteady lifts and wakes of oscillating rectangular prisms, Proc. ASCE: J. Eng. Mech. Div. 101(EM6) (1975) 855–871.
[36] A. Okajima, Strouhal numbers of rectangular cylinders, J. Fluid Mech. 123 (1982) 379–398.
[37] A. Kareem and J.E. Cermak, Pressure fluctuations on a square building model in boundary-layer flows, J. Wind Eng. Ind. Aerodyn. 16 (1984) 17–41.
[38] A. Kareem, C.-M. Cheng and P.C. Lu, Pressure and force fluctuations on isolated circular cylinders of finite height in boundary layer flows, J. Fluids Struct. 3 (1989) 481–508.
[39] M. Loeve, Probability Theory, 4th Ed. (Springer, New York, 1977).
[40] T. Miyata and M. Miyazaki, Turbulence effects on aerodynamic response of rectangular bluff cylinders, in: Wind Engineering Proc. 5th Int. Conf., Fort Collins, Colorado, USA, ed. J.E. Cermak (1979) pp. 631–642.
[41] T. Mizota, H. Yamada, Y. Kubo, A. Okajima, C.W. Knisely and H. Shirato, Aerodynamic characteristics of fundamental structures, Part 1, Section 2, J. Wind Eng. 36 (1988) 50–52 [in Japanese].
[42] A. Okajima, Aerodynamic characteristics of fundamental structures (Part 2), Section 4.1.2, J. Wind Eng. 38 (1989) 62–63 [in Japanese].
[43] P.J. Roache, Perspective: a method for uniform reporting of grid refinement studies, J. Fluids Eng. 116 (1994) 405–413.
[44] P.J. Mason and N.S. Callen, On the magnitude of the subgrid-scale eddy coefficient in large-eddy simulation of turbulent channel flow, J. Fluid Mech. 162 (1986) 439–462.